Influence of ceramic freeze-casting temperature on the anisotropic thermal expansion behavior of corresponding interpenetrating metal/ceramic composites

Siddhartha Roy, Pascal Albrecht, Kay André Weidenmann

Angaben zur Veröffentlichung / Publication details:

Roy, Siddhartha, Pascal Albrecht, and Kay André Weidenmann. 2023. "Influence of ceramic freeze-casting temperature on the anisotropic thermal expansion behavior of corresponding interpenetrating metal/ceramic composites." *Journal of Materials Engineering and Performance* 32 (19): 8795–8806. https://doi.org/10.1007/s11665-022-07769-2.

Influence of Ceramic Freeze-Casting Temperature on the Anisotropic Thermal Expansion Behavior of Corresponding Interpenetrating Metal/Ceramic Composites

Siddhartha Roy, Pascal Albrecht, and Kay André Weidenmann

Interpenetrating phase metal/ceramic composites (IPC) offer an optimum combination of strength, stiffness, wear resistance, and thermal properties. Ceramic preforms fabricated by freeze-casting are optimum for IPC fabrication due to the lamellar open porous structure of the preforms and their excellent permeability for melt infiltration. While the thermal properties of IPCs based on freeze-cast ceramic preforms have been sporadically studied, to the best of our knowledge, this is the maiden work where the influence of ceramic preform's freeze-casting temperature and preform anisotropy on the thermal expansion behavior of the resulting IPC has been systematically investigated. Preforms were freeze-cast at two different temperatures, − 10, and − 30 °C. Thermal expansion behavior was studied by thermal cycling at a slow rate between room temperature and 500 °C. Both thermal strain and coefficient of thermal expansion (CTE) were determined as a function of temperature along the freezing direction and along a direction orthogonal to it. Elastic anisotropy present in the composite samples was estimated prior to the thermal expansion measurements using a non-destructive ultrasonic technique. The results showed that the lamellar anisotropic preform structure and corresponding elastic anisotropy had a strong influence on the composite's thermal expansion behavior—generally, the highest thermal strain and CTE were achieved along the most compliant direction. The measured CTE values were compared with relevant analytical models.

Keywords elastic anisotropy, freeze-casting, interpenetrating structure, metal/ceramic composites, thermal expansion

1. Introduction

Metal/ceramic composites with an interpenetrating structure (IPC) possess a co-continuous and three-dimensional percolating network of both metallic and ceramic phases (so-called 3-3 connectivity as proposed by Newnham (Ref 1)). IPCs offer several advantages over other composite morphologies such as particle reinforced as well as long and short fiber-reinforced composites. These include a good combination of strength and toughness, reasonably high stiffness and wear resistance, lower thermal expansion along all directions, near isotropic characteristics, etc. (Ref 2-4). Moreover, in IPCs it is also readily possible to tailor the properties by varying the morphologies of the individual phases. IPCs are typically fabricated by infiltration of liquid metal in an open porous ceramic body (known as preform). Several different processing routes have been successfully employed in the last several years to fabricate open porous ceramic preforms suitable for the fabrication of IPCs (Ref 5, 6). Among the processing routes employed to fabricate the porous ceramic bodies, freeze-casting has been used rather extensively in recent years (Ref 7-13). Preforms fabricated by freeze-casting and drying possess a typical domain structure with each domain consisting of parallel ceramic lamellae. Such preforms offer several attractive features, e.g., environment-friendly processing route, presence of a wide range of open porosity with excellent permeability for successful melt infiltration to fabricate composites, sufficient mechanical strength after sintering as well as ease of varying both the ceramic content and ceramic phase morphology for tailor-made structure and properties (Ref 14-19).

Considering the unique microstructure of freeze-cast porous ceramics and metal/ceramic composites based on them, several recent studies have been carried out on these composites. Shaga et al. (Ref 20) combined freeze-casting and pressureless infiltration to fabricate interpenetrating Al-Si-Mg/SiC composites with up to 40 vol.% SiC. The composite with 30 vol.% SiC yielded the highest compressive strength of 722 MPa along the freezing direction. The elastic constants along longitudinal and transverse directions were determined from the measured

Siddhartha Roy, Institute for Applied Materials (IAM-WK), Karlsruhe Institute of Technology, 76131 Karlsruhe, Germany; and Department of Metallurgical and Materials Engineering, Indian Institute of Technology Kharagpur, Kharagpur 721302, India; **Pascal Albrecht**, Institute for Applied Materials (IAM-WK), Karlsruhe Institute of Technology, 76131 Karlsruhe, Germany; and and **Kay André Weidenmann**, Institute for Applied Materials (IAM-WK), Karlsruhe Institute of Technology, 76131 Karlsruhe, Germany; and Institute of Materials Resource Management, University of Augsburg, 86135 Augsburg, Germany. Contact e-mail: siddhartha@metal.iitkgp.ac.in.

ultrasound velocities. The highest Young's modulus of 163 GPa was measured for the composite with 40 vol.% SiC. As the density of the composite was only 2.87 g/cc, the specific stiffness of the composite was almost 57 GPa/(g/cc). Guo et al. (Ref 21) also fabricated Al-Si-Mg/Al_2O_3.ZrO_2 IPCs by freeze-casting and pressureless infiltration. The total ceramic content was maintained constant, while the ratio of Al_2O_3:ZrO_2 was varied. The composition of the ceramic mixture, lamellar structure, and the extent of interfacial reaction controlled the strength of the composite. The highest compressive strength and bending strength were achieved in the composites with the lowest Al_2O_3 content in the porous ceramic composite preform. Qi et al. (Ref 9) used ultrasonic-assisted spontaneous infiltration of Zn-5Al in freeze-cast ZrB_2-SiC preforms to fabricate IPCs. The resulting mechanical properties continuously improved with the increasing duration of the ultrasonic casting. After a duration of 300 s, the measured flexural strength, compressive strength, and fracture toughness were 225, 210, and 3 MPa√m, respectively. In further work, Guo et al. (Ref 22) pressure-infiltrated Al in freeze-cast Al_2O_3-ZrO_2 preforms to fabricate IPCs. In composites with 41 vol.% ceramic, the achieved flexural strength and K_{IC} fracture toughness were 293 and 9.0 MPa√m, respectively. With increasing ceramic content and sintering temperature, the ceramic lamellae became more compact. This reduced the content of brittle Al_3Zr and correspondingly the strength and fracture toughness of the IPC increased. Ferraro et al. (Ref 23) fabricated metal/ceramic microlaminates through pressureless infiltration of Al-4Mg in freeze-cast alumina preforms. The composites exhibited a good combination of strength and toughness with a flexural strength of 735 MPa and 3-point bending fracture toughness of 15.6 MPa√m. In a recent study, Roy et al. (Ref 24) studied the effect of freeze-casting temperature and melt infiltration technique on stiffness and compressive strength of Al-12Si/Al_2O_3 freeze-cast composites. Squeeze-casting and die-casting were employed to infiltrate the freeze-cast ceramic preforms. A reduction in the freezing temperature of the preforms yielded a finer ceramic structure, which ultimately resulted in a significant increase in stiffness and compressive strength along the freezing direction. The measured highest compressive strength was more than 1.1 GPa. The domain-level mechanical properties, as well as the influence of the domain orientation on the stiffness, compressive strength, deformation behavior, and internal load transfer mechanism of IPCs based on freeze-cast ceramic preforms, were also studied in several research articles (Ref 25-28). These studies confirmed that the individual domains of the IPC displayed pronounced anisotropy—being stiff, strong, and quasi-brittle along the ceramic lamellae (ceramic controlled behavior) and compliant, soft, and ductile transverse to the lamellae (metallic alloy controlled behavior). Further, when mechanically loaded, significant load transfer occurred from the softer and more compliant metallic phase to the ceramic through the strong metal/ceramic interphase. As the metallic alloy started undergoing plastic deformation, the extent of load transfer increased even further and the highest stress borne by the ceramic phase was more than double that of the applied stress. A thorough treatment of the mechanism of internal load transfer is available in a recent review article (Ref 29).

Owing to the higher melting points and thermal conductivities of metals over polymers, composites based on metallic matrix offer much improved high-temperature properties and creep resistance than polymer matrix composites (Ref 30, 31). Furthermore, composites' thermal properties depend strongly upon the reinforcement content and its morphology, distribution, and orientation. As the morphology and content of the ceramic phase in freeze-cast preforms can be widely varied, metal/ceramic composites based on these preforms can potentially be very attractive for thermal management applications. Despite this strong motivation, only a few studies have been reported so far on the thermal properties of IPCs based on freeze-cast ceramic preforms (Ref 32-35). Hautcoeur et al. (Ref 33) studied the thermal conductivity of IPCs fabricated by infiltration of aluminum alloy melt in freeze-cast alumina and zirconia preforms. The composites displayed a large anisotropy with high thermal conductivity parallel to the freezing direction and much lower thermal conductivity perpendicular to it. Tang et al. (Ref 34) fabricated Al_2O_3/Cu heat dissipation substrates by freeze tape casting and melt infiltration. Both thermal conductivity and thermal expansion coefficient decreased with increasing alumina content. The heat dissipation property of the LED modules with the fabricated IPC substrates was considerably better than the commercially available modules with pure alumina substrates. Nakata and Suganuma (Ref 35) first fabricated porous alumina preforms with 15-70 vol.% porosity by gelate-freezing and particle sintering, and subsequently, alumina/Al IPCs were fabricated by squeeze-casting. Both thermal conductivity and coefficient of thermal expansion (CTE) of the IPCs increased with increasing Al-content.

The foregoing discussion shows that a systematic study of the influence of structural anisotropy and lamellae size on the thermal expansion behavior of IPCs based on freeze-cast ceramic preforms is still lacking. In some previous relevant works (Ref 32, 36, 37), we studied the thermal expansion behavior in some Al-Si alloy/alumina IPCs. The primary aim of these studies was to ascertain the influence of the ceramic content and morphology on the thermal expansion behavior, especially on the CTE. In (Ref 37), open porous alumina preforms were fabricated using polymer waxes as pore formers. These preforms were infiltrated using Al-12Si alloy to fabricate IPCs with alumina content between 30 and 40 vol.%. With increasing alumina content, the CTE of the IPC decreased continuously. The measured CTEs were compared with different analytical models and the Schapery upper bound was the most accurate. Similar IPCs fabricated based on porous alumina preforms using cellulose fibers as pore formers were studied in (Ref 36). The green bodies for the porous preforms were fabricated by uniaxial pressing of mixtures of alumina powders and cellulose fibers, used as pore formers. This uniaxial pressing of the powder mixtures rendered the prefroms to behave as transverse isotropic materials having lower stiffness along the preform press direction. CTE measurement of the IPCs along the three orthogonal directions showed that the thermal expansion behavior of the IPCs was also transverse isotropic—highest thermal expansion was observed along the direction of the lowest stiffness. Finally, in (Ref 32) we studied the influence of phase morphologies at similar ceramic contents through direct comparison between IPCs having a random structure and iPCs with columnar structure based on freeze-cast alumina preforms. Within the scope of this work, our aim is to carry out a detailed analysis of the influence of the freeze-casting process parameters on the thermal expansion behavior of the corresponding composites. To the best of our knowledge, this aspect of such composites has never been studied before. Some of the results reported in this work have already been published in (Ref 32); however, they have been included here

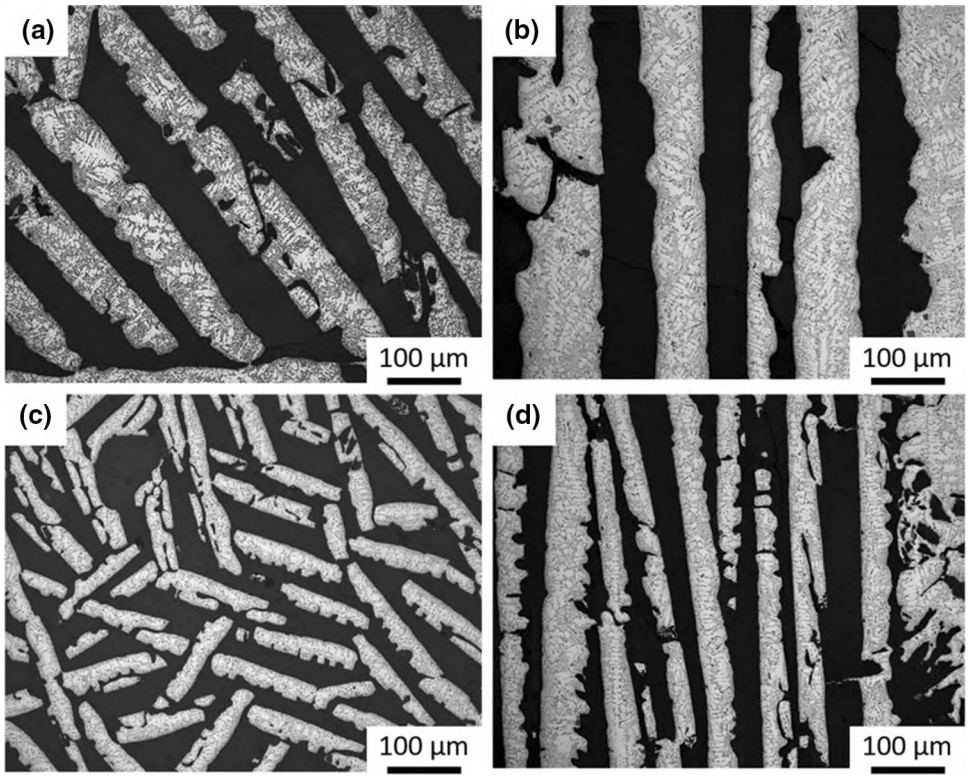

Fig. 1 Representative optical micrographs of the studied IPC samples. (a—b): Micrographs for the ceramic preform freeze-cast at − 10 °C and (c-d): micrographs for the ceramic preform freeze-cast at − 30 °C. Micrographs (a) and (c) show the faces normal to the freezing direction. Micrographs (b) and (d) show the faces parallel to the freezing direction

Table 1 Summary table for dimensions, density, ceramic content, longitudinal sound wave velocities and corresponding longitudinal elastic constants, and anisotropy ratio of the longitudinal elastic constants in the samples studied

Sample	Dimensions, mm	Density, Mg/m^3	Ceramic content, vol.%	V_L, m/s	V_{T1}, m/s	V_{T2}, m/s	$C_{ii,L}$, GPa	$C_{ii,T1}$, GPa	$C_{ii,T2}$, GPa	AR
Al-12Si	4 × 6.75 × 4.15	2.68	…	6767 ± 45	6733 ± 26	6760 ± 9	123	122	123	0
IPC-10, F	6.88 × 4.18 × 4.11	3.14	41	8401 ± 91	7399 ± 17	8124 ± 43	222	172	207	0.15
IPC-10, N	4.17 × 7.16 × 4.42	3.18	38	8319 ± 11	7823 ± 95	7656 ± 24	220	194	186	0.14
IPC-30, F	6.94 × 4.12 × 4.19	3.16	40	8525 ± 18	7689 ± 45	7498 ± 158	230	187	178	0.21
IPC-30, N	4.17 × 7.08 × 4.12	3.15	39	8530 ± 67	7396 ± 92	7712 ± 32	229	172	187	0.22

to facilitate a detailed comparison between microstructures obtained using different freeze-casting conditions.

Freeze-cast alumina preforms with similar ceramic content were first fabricated by freezing at two different sub-zero temperatures and subsequent sintering, thereby resulting in different ceramic lamellae sizes. IPCs were fabricated by infiltration of Al-12Si melt in the fabricated preforms via squeeze-casting. Thermal expansion behavior of the IPCs parallel and orthogonal to the freezing direction was measured by thermal cycling between room temperature and 500 °C at a slow heating–cooling rate within a dilatometer. The extent of processing induced structural anisotropy of the studied IPC samples was determined by non-destructive ultrasonic modulus measurement prior to dilatometer measurements. The CTE evolution in different samples and along various directions has been compared with different analytical model predictions.

2. Experimental Procedure

2.1 Sample Fabrication and Microstructural Characterization

A detailed description of the processing route and microstructural characterization of the porous ceramic preforms, as well as the IPCs, is available in several earlier publications (Ref 17, 24-26). Hence, only the information absolutely relevant to the present work is mentioned here

briefly. Two types of alumina preforms were produced at the Institute for Applied Materials—Ceramic Materials and Technologies (IAM-KWT), Karlsruhe Institute of Technology, Germany, via freeze-casting and subsequent sintering. The initial ceramic content in the slurry was 22 vol.%, and freeze-casting was carried out at two different temperatures of – 10 °C and – 30 °C to obtain different lamellae sizes in the preforms. The nominal dimensions of the fabricated preforms were 10 × 44 × 66 mm^3. IPCs were fabricated by infiltrating Al-12Si melt in the porous preforms by squeeze-casting under an applied pressure of 100 MPa. Squeeze-casting was carried out at the Institute of Surface Technology and Materials Science at Aalen University of Applied Sciences, Aalen, Germany.

SEM images of the porous alumina preforms have already been published in (Ref 24, 26). These preforms display a characteristic porous lamellar structure and ceramic bridges connecting the lamellae. Representative optical micrographs of the infiltrated IPCs are shown in Fig. 1. In this figure, the micrographs (a-b) and (c-d) belong to the IPCs based on the alumina preforms freeze-cast at – 10 °C (hereafter named IPC-10) and – 30 °C (hereafter named IPC – 30), respectively. While micrographs (a) and (c) correspond to the face orthogonal to the preform freezing direction, micrographs (b) and (d) correspond to the faces parallel to the freezing direction. In all the micrographs, the darker regions denote the alumina ceramic

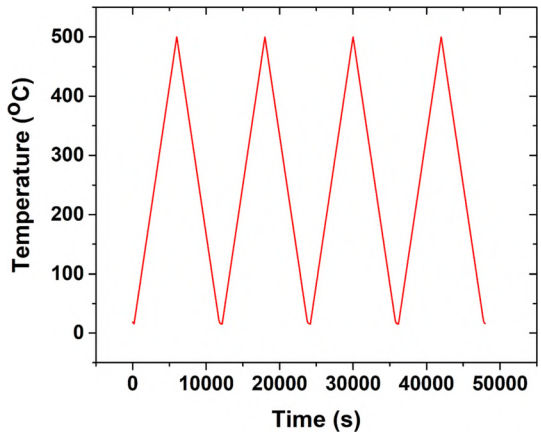

Fig. 2 Temperature vs. time profile followed during the measurement of thermal strain in dilatometer

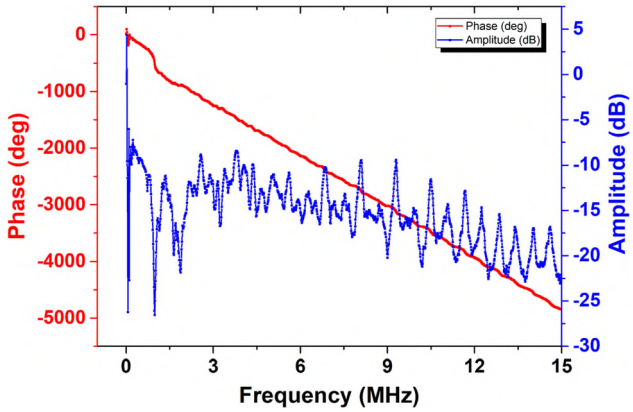

Fig. 3 Representative phase-frequency and amplitude-frequency spectra obtained from UPS of one IPC sample

while the lighter regions correspond to the near eutectic metallic alloy Al-12Si. As the solubility of Al in Si is zero at all temperatures, the microstructure of the metallic alloy consists of Al-rich primary α-phase and pure Si particles. The microstructures of the faces normal to the freezing direction in both IPC types show an alternating lamellar structure. Due to the lower freezing temperature of the preform freeze-cast at – 30 °C, the lamellae in IPC–30 are much finer. The lamellae thickness in both IPC types on the face normal to the freezing direction was measured using the software ImageJ. The average lamellae thickness ± standard deviation for the two IPCs IPC-10 and IPC-30 was measured to be 35 ± 13 μm and 22.5 ± 8 μm, respectively. As the ceramic lamellae grow on the cold substrate surface along the freezing direction, along the freezing direction the lamellae are mostly continuous. The thicknesses of these continuous lamellae on the plane parallel to the freezing direction do not represent the actual lamellae thickness, as it depends upon the orientation of the lamellae and the angle at which they section the plane of observation (Ref 25). Detailed SEM analysis of the microstructure as well as the study of the in situ damage evolution under compression within an SEM (Ref 26) has confirmed that the interfacial bonding between the metallic and ceramic lamellae is strong. When compressed along the freezing direction, failure of the IPCs occurred by ceramic crushing while the interfacial regions remained mostly unaffected until significant damage occurred. The amount of residual porosity in the IPCs was measured via the Archimedes principle and micro-computed tomographic (μCT) analysis. The residual porosity in IPC-10 and IPC-30 was found to be almost 3% and 0.5%, respectively (Ref 28).

Five cuboid-shaped samples were studied in this work—one unreinforced Al-12Si sample and two samples each of IPC – 10 and IPC – 30. The Al-12Si sample was cut from the excess metallic region of one of the cast composites to ensure that it has undergone the same thermal and processing history. Hence, the behavior of this sample can be considered representative of Al-12Si in the composite. The samples had nominal dimensions of 4 × 4 × 7 mm^3. The change in sample length during the dilatometer measurements was carried out along the longest dimension in each sample. Table 1 summarizes the dimensions, density, and ceramic content of the samples studied. Ceramic content was measured assuming the absence of any residual porosity.

2.2 Measurement of Longitudinal Elastic Constants Using Ultrasound Phase Spectroscopy (UPS) Method

The longitudinal elastic constants along the three mutually orthogonal directions in each cuboid sample were measured using the non-destructive ultrasound phase spectroscopy (UPS) technique. The theoretical background of this technique has been discussed in detail in several recent publications (Ref 38, 39) and will not be repeated. In this technique, a continuous, harmonic, and sinusoidal ultrasonic wave is transmitted through the sample and the phase shift of the propagating wave is measured as a function of frequency. One network analyzer (Advantest 3754A) and two identical broadband ultrasonic longitudinal wave transducers (Panametrics V122 with a central frequency of 5 MHz) were used for measurement purposes, with one transducer acting as a transmitter and the second transducer acting as a receiver. A water-soluble couplant was used between the transducers and the sample to facilitate the propagation of ultrasound in the sample. To define the

co-ordinate system for ultrasonic measurements, in each sample the freezing direction was denoted as "L" and the two directions normal to the freezing direction were denoted as "T1" and "T2," respectively. For a non-dispersive sample, the slope of the phase-frequency spectrum yields a straight line with a quasi-constant slope. The sound velocity along any direction i (V_{ii}) can be determined from the sample length and the measured constant slope of the phase-frequency spectrum. The corresponding elastic constant can be determined from the sound velocity according to the relation

$$C_{ii} = \rho \cdot V^2 \qquad \text{(Eq 1)}$$

where ρ is the sample density. In this study, each measurement was repeated thrice and their average ± standard deviation is reported.

2.3 Dilatometer Measurements

Thermal expansion measurement studies were performed at the Institute of Applied Materials (IAM-WK), Karlsruhe Institute of Technology, Germany. A dilatometer of type DIL 805A/D from Bähr-Thermoanalyse GmbH, Hüllhorst, Germany, was used to measure the length change of the samples as a function of temperature during both heating and cooling. A thorough description of the experimental procedure is available in (Ref 40). Length change was measured along the long axis of each sample studied. Hereafter, for the samples undergoing dilatometer experiments, the direction parallel to the freezing direction in each IPC sample will be marked with "F" and the direction normal to the freezing direction will be marked with "N." Out of the two normal directions, dilatometer experiments were carried out only along one direction. The directions "F" and "N" correspond to directions "L" and "T_1 or T_2" of ultrasonic experiments, respectively. For thermal expansion measurements, the sample was placed between two alumina pushrods. One pushrod was fixed, and the other pushrod was connected to a linear variable differential transformer (LVDT) to measure the sample length change precisely. The two opposite faces of the samples along the direction of length change measurement, which were in touch with the pushrods, were polished well prior to the experiments to ensure plane parallelism. A thermocouple of type S was spot welded to the sample prior to the experiment to continuously record the sample temperature. During the experiment, the sample was placed in the center of an induction coil and the dilatometer chamber was filled with inert helium gas. For each sample, four thermal cycles (both heating and cooling) were carried out between room temperature and 500 °C at a constant heating/cooling rate of 5 °C/min. Temperature-time profile followed during dilatometer measurements are shown in Fig. 2.

3. Results and Discussions

Figure 3 shows representative phase-frequency and amplitude-frequency spectra obtained from UPS of one IPC-10 sample measured along the freezing direction. Similar spectra were obtained for all other samples studied in this work. The figure shows that over the complete frequency range, the phase spectrum (red curve) has a quasi-constant slope. This proves that the samples are non-dispersive and sound velocity is independent of frequency. The amplitude spectrum oscillates in a regular fashion and decreases continuously with increasing frequency due to an increase in attenuation. However, even at the highest frequency of 15 MHz studied in this work, the amplitude remains at a reasonably high value, confirming that the measured signal strength is sufficiently high throughout. According to Wanner (Ref 41), the amplitude spectrum is an important measure of signal quality. While amplitude always decreases with increasing frequency, a large drop beyond a limiting frequency denotes that no measurement is possible above that frequency.

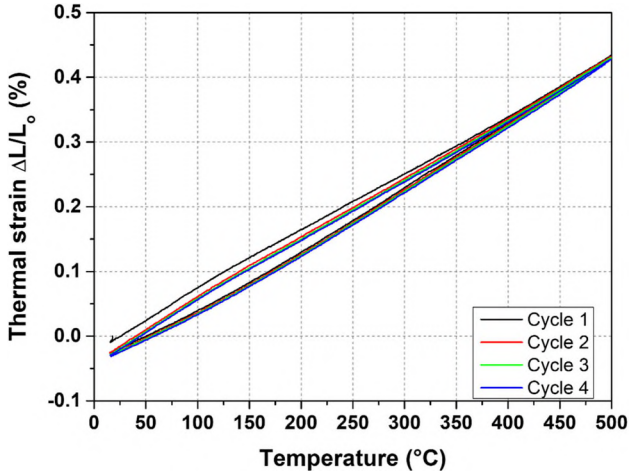

Fig. 4 Plot of thermal strain vs. temperature during the four dilatometer cycles in the IPC-30 sample along F direction

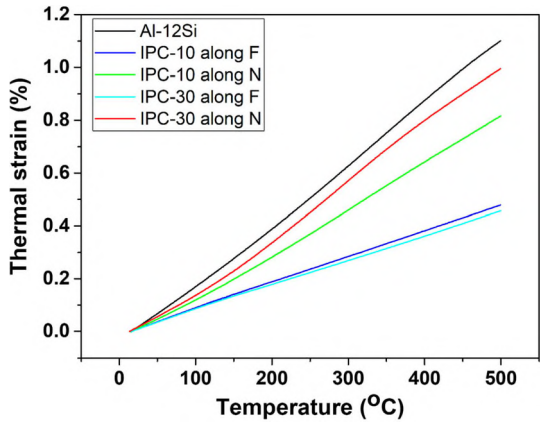

Fig. 5 Plot of thermal strain vs. temperature during the second heating path in all studied samples

The measured sound velocities and the longitudinal elastic constants determined therefrom along the three orthogonal directions in each studied sample prior to the dilatometer experiment are provided in Table 1. In an isotropic material, identical elastic constants are obtained along all directions of a sample, while in anisotropic materials, different elastic constants are obtained in different directions (Ref 42, 43). Table 1 shows that, as expected, unreinforced Al-12Si is elastically isotropic. All the IPC samples studied are elastically anisotropic. As previously shown in (Ref 24, 25), due to the continuous ceramic lamellae along the freezing direction, in each composite sample the highest elastic constant is obtained

along this direction (i.e., $C_{ii,L}$). The elastic constants along the two transverse directions ($C_{ii,T1}$ and $C_{ii,T2}$) are lower and depend upon the orientation of the ceramic lamellae with respect to the measurement direction. If the relative lengths of the lamellae are small with respect to the sample dimensions and they are oriented randomly, the elastic constants along the two transverse directions should be similar and the IPC should be treated as transversely isotropic material. In fact, it is observed that due to the much finer lamellae size in IPC-30, for these composite samples the difference between $C_{ii,T1}$, and $C_{ii,T2}$ is smaller than that in IPC-10. As the elastic anisotropy of composites plays a major role in its thermal expansion behavior, the anisotropy ratio (AR) has been defined in this work as

$$\mathrm{AR} = \frac{C_{ii,L} - \mathrm{average}\left(C_{ii,T1}, C_{ii,T2}\right)}{C_{ii,L}} \quad \text{(Eq 2)}$$

The corresponding AR values in the studied samples are also shown in Table 1. For unreinforced Al-12Si sample, AR = 0. The extent of elastic anisotropy in IPC-30 is almost 50% higher than that in IPC-10 (AR ≈ 0.21 for IPC-30, while for IPC-10, AR ≈ 0.14). This results from the higher $C_{ii,L}$ in IPC-30 samples caused by the much finer lamellae size.

Figure 4 shows plots of thermal strain vs. temperature along the freezing direction in IPC freeze-cast at − 30 °C, respectively. The plot is representative of all the samples studied in this work in the fact that the highest thermal hysteresis and residual thermal strain at the completion of the cycle were observed after the first cycle. The subsequent cycles (cycles 2-4) displayed significantly reduced thermal hysteresis—the heating and cooling cycles showed almost closed form shapes and the strain increment was almost zero. Due to the large CTE difference between the constituents (Al-12Si and Al_2O_3) of the IPC, significant thermal residual stresses are generated in such composites during cooling after melt infiltration. Due to the lower CTE of the ceramic phase, in the as-fabricated samples, Al_2O_3 should have compressive residual stresses, and to balance it, the residual stress state in Al-12Si should be tensile (Ref 29, 44). The first heating–cooling cycle is strongly affected by the processing-induced residual stresses in the samples, and hence, the observed behavior is not representative of the actual samples. After the first cycle, due to the slow heating–cooling rate, the samples have annealed, the residual stresses have stabilized, and correspondingly, the trend observed during cycles 2-4 is more representative of the actual behavior. Similar cyclic thermal strain evolution has been observed in several previous research articles involving a wide range of reinforcement phase morphologies (Ref 36, 37, 45). Correspondingly, the evolution of the thermal strain during the second heating path and the average CTE during the heating paths of cycles 2–4 will be used in this work for further discussion.

Figure 5 shows the evolution of thermal strain vs. temperature for the second heating path in all the samples studied. An identical trend was observed during heating paths 3 and 4. The plot shows that, as expected, the highest thermal strain was experienced by the unreinforced Al-12Si sample. The addition

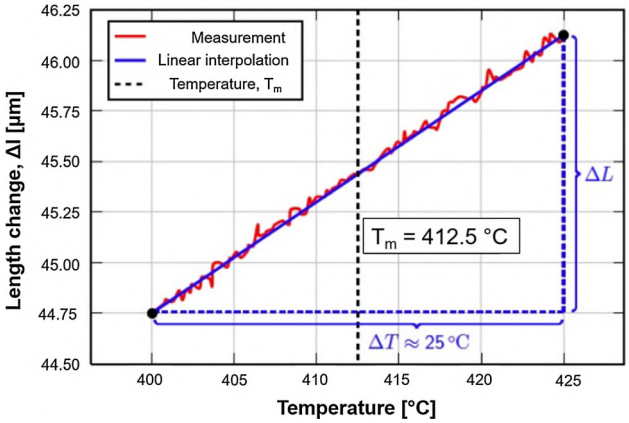

Fig. 6 Methodology followed to determine the CTE of the samples at the midpoint of each 25 K interval

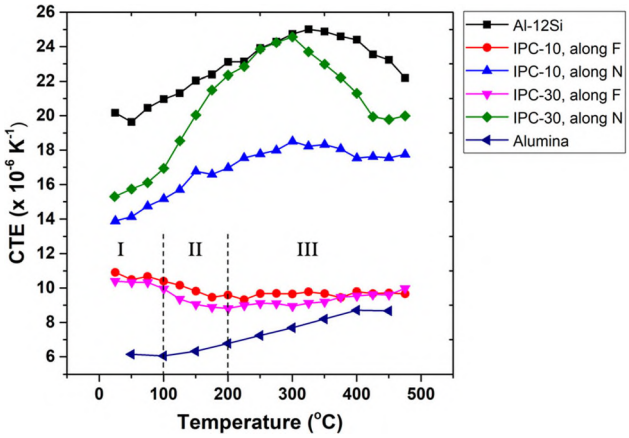

Fig. 7 Plot showing the evolution of CTE vs. temperature during the heating path for the samples studied in this work. The data points for alumina have been taken from (Ref 53)

Table 2 Material parameters used to calculate the analytical model expressions for CTE of the composites at 50 and 300 °C

	Young's modulus, E , GPa	Shear modulus, G, GPa	Bulk modulus, K, GPa	Poisson's ratio, v	CTE, × 10^{-6}/K
At 50 °C					
Al-12Si	74.4	27.97	72.94	0.33	19.8
Al_2O_3	398.45	160.97	255.42	0.24	6.1
At 300 °C					
Al-12Si	62.7	23.40	65.31	0.34	24.8
Al_2O_3	385.5	155.46	247.14	0.24	7.7

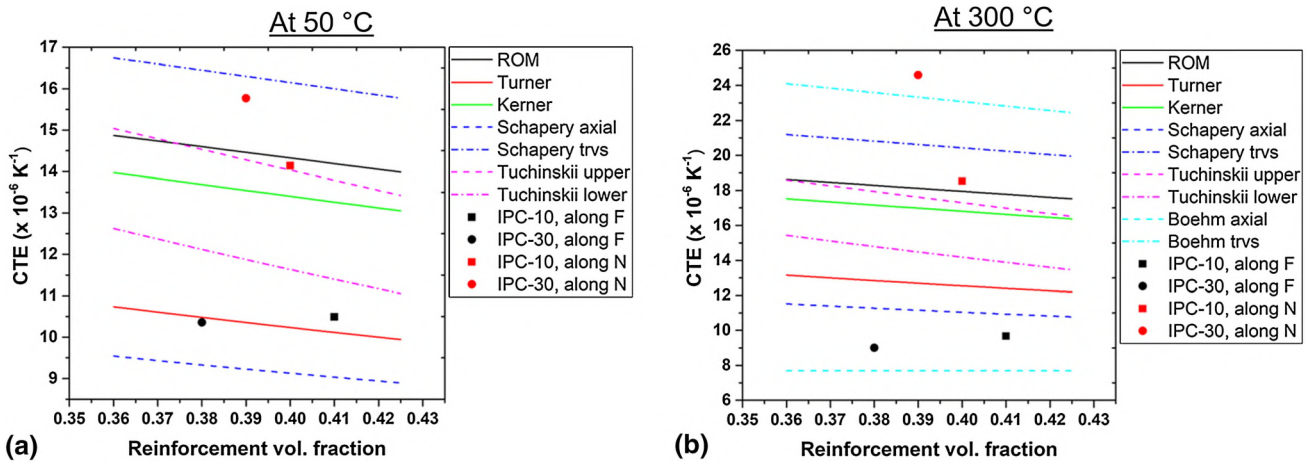

Fig. 8 Comparison of the experimentally determined CTE values of the studied IPC samples with relevant analytical models—(a): at 50 and (b): at 300 °C

of the ceramic reinforcement reduces the thermal strain due to its obvious higher stiffness and corresponding strong constraining effect to the unhindered thermal expansion of Al-12Si. However, the IPC samples display strong direction-dependent anisotropy of thermal strain. Significantly lower thermal strains are observed in the IPC samples along the preform freezing direction (i.e., direction F), while along the normal directions the thermal strains are considerably higher.

The prevalent thermal strain anisotropy can be attributed to different residual stress states and the temperature-dependent flow behavior of Al-12Si and Al_2O_3. As already discussed, in the as-fabricated condition, the residual stresses in Al-12Si should be tensile in nature while within Al_2O_3, the residual stresses should be compressive. During re-heating, Al-12Si would try to expand more due to its higher CTE which would be impeded by the presence of the high volume content of stiff Al_2O_3. This would induce compressive stresses in Al-12Si. With continued heating, initially, these CTE mismatch-induced compressive residual stresses in Al-12Si would act to cancel out the processing-induced tensile residual stresses. At even higher temperatures, compressive stresses in Al-12Si would increase further. In metal/ceramic composites, the situation is rendered even more complicated due to different flow behaviors of its constituents. While Al_2O_3 would remain elastic throughout, for Al-12Si, the yield stress would decrease with increasing temperature. Correspondingly, at some point during the heating of the composite, Al-12Si would undergo plastic deformation. As during plastic deformation metallic alloys behave as incompressible solids (i.e., volume remains constant and Poisson's ratio = 0.5 (Ref 46)), this would essentially mean that if the volume expansion along any one direction is hindered, the expansion would be higher along the other directions (ideally, for an isotropic material, such as polycrystalline metals and their alloys in the absence of texture, expansion coefficient is same along all directions and volumetric expansion coefficient (β) is three times the linear expansion coefficient (α) (Ref 47). In the IPCs under study, the continuous Al_2O_3 lamellae along the F direction and the strong interfacial bonding present between Al-12Si and Al_2O_3 (as already documented by in situ SEM compression tests in (Ref 26) would operate together to constrict the thermal expansion of Al-12Si along this direction, and as a result, the overall thermal strain in the IPCs along the F direction would be smaller. To satisfy the constant volume criterion, expansion of Al-12Si will be much more pronounced along the orthogonal N directions and this would consequently lead to the observed much higher thermal strains of the IPCs along these directions. Similar thermal strain anisotropy has already been reported in different metal/ceramic composites with aligned reinforcements, such as unidirectional fiber-reinforced composites (Ref 48), short-fiber reinforced composites (Ref 49-51), layered composites (Ref 45), as well as some IPCs with anisotropic preform stiffness (Ref 52).

To determine the progressive evolution of CTE with temperature, the average of the length change vs. temperature plots during heating paths 2–4 was first discretized into intervals of 25 K each. For each interval, a straight line was fitted to the plot and its slope was determined. Finally, the CTE corresponding to the mean temperature of each such interval was determined according to:

$$\alpha = \frac{1}{l_0} \cdot \frac{dl}{dT} \qquad \text{(Eq 3)}$$

where l_0 is the length of the sample along the measurement direction at the start of each interval and (dl/dt) is the slope of the length change vs. temperature plot determined for each interval, as discussed above. A schematic explaining the methodology followed to determine the CTE at the midpoint of each interval is shown in Fig. 6.

Figure 7 shows the evolution of calculated CTE vs. temperature in the samples studied. For comparison purposes, data points for CTE of pure alumina at different temperatures are also shown. These are literature values taken from (Ref 53). The figure shows that the CTE of unreinforced Al-12Si increases from about 20×10^{-6} /K to the highest value of approx. 25×10^{-6} /K between 300 and 350 °C. At even higher temperatures, the CTE of unreinforced Al-12Si continuously decreases. Similar temperature-dependent CTE evolution in Al-Si alloys has been reported in numerous publications (Ref 45, 52, 54), and according to the original work by Hahn and Armstrong (Ref 55), the reduction in CTE at temperatures $>$ 300 °C may be attributed to the re-dissolution of Si in Al.

As with thermal strain evolution in Fig. 5, the CTE evolution in the IPC samples also displays a pronounced anisotropy. In both IPC types,

- much lower CTE values are obtained along the F-direction approaching the CTE of pure Al_2O_3
- Along the N-direction, the CTE values are considerably higher and the shapes of the plots qualitatively resemble unreinforced Al-12Si

In the following, the different CTE evolution behavior along the F- and N-directions will be treated separately.

CTE evolution along the F-direction.

Along the F-direction, the CTE evolution curves for the IPC-10 and IPC-30 samples almost superimpose over each other. As shown in Fig. 7, the curves can be divided into three regions. In region I, the CTE values are approx. constant and lie at reasonably high values between 10 and 11 $\times$ 10^{-6} /K. Both Al-12Si and Al_2O_3 are undergoing elastic deformation in this region which continues up to $\approx$ 100 °C. In region II, a slight reduction in CTE by around 2 $\times$ 10^{-6} /K occurs in both IPC samples. This change in behavior can be attributed to the onset of plastic deformation in Al-12Si under CTE-mismatch-induced reverse compressive stresses, as already discussed. With a further increase in temperature in this region, the plastically deforming metallic phase flows into the residual pores available in the IPC after infiltration, thereby closing those pores and concomitantly reducing the CTE further. Similar pore closure phenomena in IPCs by the plastically deforming metallic phase, resulting in a reduction in CTE, have been reported in several studies (Ref 54, 56–58). Region II ends at approx. 200 °C. Finally, with further increasing the temperature in region III, the CTE remains approx. constant at a value of 9 $\times$ 10^{-6} /K and slowly approaches the CTE of pure Al_2O_3 at even higher temperatures. The metallic phase is now extremely soft and has almost no influence on the expansion behavior of the IPCs along the F-direction. The thermal expansion of the IPC is now almost completely dependent upon the continuous Al_2O_3 lamellae. The behavior is similar to the axial CTE evolution in unidirectional continuous fiber-reinforced composites, as modeled by Böhm et al. (Ref 57).

CTE evolution along the N-direction.

A completely different CTE evolution is observed along the N-direction. In line with the higher thermal strain experienced by the samples along this direction, the calculated CTE values are also significantly higher. This may be attributed to the already explained higher dilation of the plastically deforming metallic matrix along these directions in comparison with the F-direction. The fact that in Fig. 7 the CTE along the N-direction suddenly increases at the beginning of region II discussed above (onset of plastic deformation of Al-12Si) further corroborates this. Overall, the shapes of the curves of CTE evolution in the IPCs along the N-direction follow the shape of unreinforced Al-12Si. This confirms that the thermal expansion of the IPCs along the N-direction is controlled by the expansion behavior of the more compliant and softer metallic phase itself. Despite the obvious similarities, there is a striking difference in the CTE evolution behavior shown by the two IPC samples. Much higher CTE values are obtained for IPC-30, with the values even reaching up to the CTE values for unreinforced Al-12Si. The reason behind this stark difference may be attributed to several factors. One reason could be the structural difference between individual composite samples. As shown in the optical micrographs of Fig. 1, the IPCs are inherently inhomogeneous, especially the lamellae orientation plays a big part in the transverse plane (= the strain measurement direction for the dilatometer study along the N-direction). As the Al_2O_3 content of the samples was similar, this is not expected to play a big role. However, probably the biggest factor is the difference in the degree of elastic anisotropy present in the two IPC samples measured along the N-direction. As shown in Table 1, while the anisotropy ratio (AR) is 0.14 in the IPC-10 sample, the same value is 0.22 (more than 50% higher) in the IPC-30 sample. This essentially means that the IPC-30 sample was relatively much stiffer along the F-direction, and correspondingly, as plastic deformation starts in Al-12Si, the expansion of the metal along the F-direction would be more strongly restricted, thereby enhancing its thermal expansion along the orthogonal N-direction. This would explain the considerably higher CTE of the IPC-30 sample.

A host of analytical models have been developed to predict the CTE of composite materials based on the morphology and volume content of the constituent components and their individual thermomechanical properties. Some of the well-established models include the Rule of Mixtures (ROM) (Ref 59), Turner model (Ref 60), Kerner model (Ref 61), Tuchinskii model (Ref 62), and Schapery upper and lower bounds (Ref 63). A detailed description of these models is outside the scope of this work and can be obtained from the cited references. A general application of these models to predict the overall thermal expansion behavior of the metal/ceramic composites is, however, complicated. This is primarily due to the fact that while these models assume purely elastic deformation behavior of both components, in the real composite samples the metallic phase undergoes plastic deformation (as already explained before) and the ceramic phase may undergo damage. There might also be local interfacial failure, which would also have a strong influence on composite's CTE evolution, while the models assume a perfect regular microstructure and ideal interfacial bonding.

Despite these limitations, comparing the experimentally determined real CTE of the composites at different temperatures with these micromechanical models shed valuable insight into the real composites' thermal response. Among these models, the ROM model is the simplest, and according to this model, the CTE of the composite is simply the sum of the products of the vol. fraction and the CTE of the composite's constituents, assuming no porosity. The Turner model (Ref 64) is based on the assumption that within the composite there are a homogeneous strain distribution and hydrostatic stress state. An ideal interface is assumed to exist between the composite's individual components. In the special case of both constituents having the same bulk modulus, the Turner model prediction matches with the ROM model. Based on the assumption of spherical, spatially randomly distributed reinforcement particles in the matrix and from the analysis of the mean elastic strains and stresses in a composite of simple geometry, Kerner (Ref 61) derived an expression for the volumetric expansion coefficient of the composite material. Assuming homogeneity and isotropic behavior, the linear expansion coefficient of the composite is determined therefrom. Also for the Kerner model, the predicted CTE equals the ROM prediction if the bulk modulus of the two components is equal. In terms of applicability, while the Kerner model is more suitable for particulate reinforcements, the Turner model is more appropriate for composites with interpenetrating phase morphologies. Tuchinskii (Ref 62) proposed the model for the CTE of a two-phase interpenetrating composite. The unit cell of the composite consists of a regular 3D structure of the reinforcement phase embedded in the matrix. By combining many of these cells, the macroscopically isotropic composite material is created. For both matrix and reinforcement, equal Poisson's ratio was

considered. Unlike the earlier models which provide single-valued definite solutions, the Tuchinskii model provides expressions for upper and lower bounds within which the CTE of the real composite is expected to lie. Finally, Schapery (Ref 63) proposed expressions for CTE along axial and transverse directions in unidirectional fiber-reinforced composites. These calculations were based on extremum principles of thermoelasticity. In further work, Böhm et al. (Ref 57) modified the Schapery expressions for the special case of real composites at elevated temperatures where the metallic phase undergoes plastic deformation and exerts minimum influence on the axial CTE of the composite. They replaced the term for Young's modulus of the metallic matrix in the Schapery expression with the hardening modulus and further assumed this modulus to be much smaller than the Young's modulus of the reinforcement.

In this work, the comparison of the experimentally determined CTE of the studied composites samples with the predictions from the analytical models has been carried out at two different temperatures, i.e., 50 and 300 °C. The choice of these temperatures was motivated by the fact that at 50 °C, both Al-12Si and Al_2O_3 are undergoing elastic deformation and the composite finds itself in the region I of Fig. 7. In comparison, at 300 °C, in Al-12Si full plasticity has already set in and the composite finds itself in region III of Fig. 7. To compute the analytical models, the input parameters are CTE and the elastic moduli (Young's modulus, bulk modulus, Poisson's ratio) of Al-12Si and Al_2O_3 at the two temperatures of 50 °C and 300 °C. For alumina, the room temperature values of Young's modulus and Poisson's ratio were taken as 400 GPa and 0.24, respectively (Ref 65). The shear and bulk moduli were calculated from these values assuming isotropy and using the appropriate relations of elasticity. The elastic constants at higher temperatures were determined using the standard relation (Ref 66)

$$E(T) = E_{RT} \times \left(1 - 0.3 \times \frac{T - T_{RT}}{T_m}\right) \quad (4)$$

where E_{RT} is Young's modulus at room temperature, T is the actual temperature, T_{RT} is the room temperature and T_m is the melting point. For Al-12Si, the elastic constants over the complete temperature range were unknown. Hence, as in (Ref 67), the elastic constants of Al7SiMg alloy, compiled in (Ref 68), were used. Table 2 contains the values of the material parameters used for the calculation of the analytical models.

Figure 8 compares the experimentally determined CTE values with the predictions from different analytical models at two different temperatures. For the condition at 50 °C, as both Al-12Si and Al_2O_3 undergo elastic deformation, the ROM model, Turner model, Kerner model, Schapery model, and Tuchinskii model have been considered for the comparison. At 300 °C, as Al-12Si is undergoing plastic deformation, additionally the models proposed by Böhm have been considered.

The figure shows that, at 50 °C, in the F-direction, the Turner model strongly matches the experimental measurements. The lower limit of Tuchinskii provides values that are slightly higher than the measured values, while the predictions according to Schapery's model for axial CTE are significantly lower. The strong agreement with the Turner model indicates that the interpenetrating character of the composite plays a major role in determining its CTE along the freeze-casting direction when both phases are undergoing elastic deformation. Transverse to the freezing direction, the measured CTE values lie close to the upper limit of Tuchinskii, Schapery's model for transverse direction, and the ROM model. A good fit with Schapery's transverse direction model justifies the fact that the higher CTE along the N-direction is primarily caused by the lower stiffness along this direction. Further, proximity to the ROM model confirms that there is a lesser restriction to the thermal expansion of the composite along the N-direction, even when Al-12Si is undergoing elastic deformation, which again directly results from the lower stiffness along this direction.

At 300 °C, along the F-direction, both the measured CTE values lie between the predictions of the Böhm model and Schapery's model for axial CTE. While the Böhm model assumes a fully plastic matrix with negligible influence on the thermal expansion of the composite, Schapery's prediction, on the other hand, is based on the assumptions of an elastically behaving matrix. Proximity to Böhm's predicted values confirms that already at 300 °C, Al-12Si has attained full plasticity and the CTE of the IPC is controlled solely by the stiffer Al_2O_3 phase. Along the N-direction, while the CTE of the IPC-10 sample lies close to the ROM model, for the IPC-30 sample, the measured CTE lies significantly above and is marginally higher than even the prediction of Böhm's model along the transverse direction. These observations confirm that the plastically deforming Al-12Si controls the thermal expansion behavior of the composite in this direction.

4. Conclusions

Anisotropic thermal expansion behavior of Al-12Si/alumina interpenetrating phase composites was studied in this work between room temperature and 500 °C. The composites were fabricated by squeeze-casting Al-12Si melt in lamellar open porous alumina preforms fabricated via the freeze-casting process performed at two different temperatures of − 10 and − 30 °C, respectively. Due to the lower freezing temperature, the preforms freeze-cast at -30 °C were much finer. The preferred growth along the freezing direction and the ensuing lamellar microstructure resulted in pronounced anisotropy in the composites—owing to the presence of the continuous ceramic lamellae along the freezing direction, the highest stiffness was achieved along this direction. Due to the finer microstructure of the composite based on the preform freeze-cast at − 30 °C, the stiffness of this composite along the freezing direction was considerably higher, which resulted in an even higher anisotropy.

The main conclusions of this work are as follows:

- The ceramic lamellae significantly reduce the thermal strain experienced by unreinforced Al-12Si. Due to the anisotropic and lamellar structure of the freeze-cast alumina preforms, the evolution of thermal strain in the composites was also anisotropic. The continuous ceramic lamellae along the freezing direction posed a much stronger barrier to thermal expansion in this direction. As a result, thermal strain along the freezing direction of the composite was lower than directions orthogonal to it.
- As with thermal strain, the CTE evolution of the composite samples also displayed a strong anisotropy. While in the freezing direction the CTE values were low and approached the value of pure alumina, along directions normal to the freezing direction, much higher CTE values were achieved which followed the behavior of Al-12Si.

- Due to the complex lamellar morphology and the presence of strong interfacial bonding between Al-12Si and alumina, significant thermal stresses were generated in the composites which caused Al-12Si to undergo plastic deformation. In the temperature region where Al-12Si still experienced elastic deformation, the CTE anisotropy experienced by the composites was lower. However, once Al-12Si started to undergo plastic deformation, the continuous ceramic lamellae along the freezing direction strongly restricted its dilation along this direction. As the plastically deforming metallic alloy behaves as a non-compressible solid, to maintain its constant volume, the thermal expansion along the orthogonal directions would increase and this resulted in significantly higher CTE along the orthogonal directions.
- Due to the complex microstructure and continuously changing stress states with temperature, no single analytical model was able to predict the CTE of the composite over the complete range. When both Al-12Si and alumina underwent elastic deformation, the Turner model provided the best fit to the measured CTE along the freezing direction and Schapery's axial model and Tuchinskii upper bound explained the measured CTE best along the directions orthogonal to the freezing direction. When Al-12Si deformed plastically, Böhm's models and rule of mixtures model were closest to the CTE measured experimentally.

Acknowledgments

We thank co-workers at Institute for Applied Materials—Ceramic Materials and Technologies (IAM-KWT), Karlsruhe Institute of Technology, as well as co-workers at Aalen University of Applied Sciences, Aalen, Germany, for providing the specimen material.

Data Availability

Raw research data used for this publication will be made available on request.

References

1. R.E. Newnham, D.P. Skinner and L.E. Cross, Connectivity and Piezoelectric-Pyroelectric Composites, *Mater. Res. Bull.*, 1978, **13**, p 525–536. https://doi.org/10.1016/0025-5408(78)90161-7
2. M. Kouzeli and D.C. Dunand, Effect of Reinforcement Connectivity on the Elasto-Plastic Behavior of Aluminum Composites Containing Sub-Micron Alumina Particles, *Acta Mater.*, 2003, **51**, p 6105–6121. https://doi.org/10.1016/S1359-6454(03)00431-2
3. G. Roudini, R. Tavangar, L. Weber and A. Mortensen, Influence of Reinforcement Contiguity on the Thermal Expansion of Alumina Particle Reinforced Aluminium Composites, *Int. J. Mater. Res.*, 2010, **101**, p 1113–1120
4. N. Kota, M.S. Charan, T. Laha and S. Roy, Review on Development of Metal / Ceramic Interpenetrating Phase Composites and Critical Analysis of their Properties, *Ceram. Int.*, 2022, **48**, p 1451–1483. https://doi.org/10.1016/j.ceramint.2021.09.232
5. K. Sang, Y. Weng, Z. Huang, X. Hui and H. Li, Preparation of Interpenetrating Alumina-Copper Composites, *Ceram. Int.*, 2016, **42**, p 6129–6135. https://doi.org/10.1016/j.ceramint.2015.12.174
6. J.H. Eom, Y.W. Kim and S. Raju, Processing and Properties of Macroporous Silicon Carbide Ceramics: A Review, *J. Asian Ceram. Soc.*, 2013, **1**, p 220–242. https://doi.org/10.1016/j.jascer.2013.07.003
7. Y. Li, P. Shen, L. Yang and S.X.Q. Jiang, A Novel Approach to the Fabrication of Lamellar Al2O3/6061Al Composites with High-Volume Fractions of Hard Phases, *Mater. Sci. Eng. A.*, 2019, **754**, p 75–84
8. Z. Hu, P. Shen and Q. Jiang, Developing High-Performance Laminated Cu/TiC Composites through Melt Infiltration of Ni-Doped Freeze-Cast Preforms, *Ceram. Int.*, 2019, **45**, p 11686–11693
9. Y. Qi, G. Chen, Z. Li, L. Chen, W. Han and Z. Du, A Novel Approach to Fabricate Ceramic/Metal Interpenetrating Phase Composites by Ultrasonic-Assisted Spontaneous Infiltration, *Ceram. Int.*, 2021, **47**, p 2903–2907. https://doi.org/10.1016/j.ceramint.2020.09.121
10. M. Fukushima, M. Nakata, Y. Zhou, T. Ohji and Y. Yoshizawa, Fabrication and Properties of Ultra Highly Porous Silicon Carbide by the Gelation–Freezing Method, *J. Eur. Ceram. Soc.*, 2010, **30**, p 2889–2896. https://doi.org/10.1016/j.jeurceramsoc.2010.03.018
11. D. Koch, L. Andresen, T. Schmedders and G. Grathwohl, Evolution of Porosity by Freeze Casting and Sintering of Sol-Gel Derived Ceramics, *J. Sol-Gel Sci. Technol.*, 2003, **26**, p 149–152. https://doi.org/10.1023/A:1020718225164
12. F. Xue, K. Zhou, N. Wu, H. Luo, X. Wang, X. Zhou, Z. Yan, I. Abrahams and D. Zhang, Porous SiC Ceramics with Dendritic Pore Structures by Freeze Casting from Chemical Cross-Linked Polycarbosilane, *Ceram. Int.*, 2018, **44**, p 6293–6299. https://doi.org/10.1016/j.ceramint.2018.01.019
13. Z. Du, D. Yao, Y. Xia, K. Zuo, J. Yin, H. Liang and Y.-P. Zeng, The Sound Absorption Performance of the Highly Porous Silica Ceramics Prepared Using Freeze Casting Method, *J. Am. Ceram. Soc.*, 2020, **103**, p 5990–5998. https://doi.org/10.1111/jace.17300
14. K.L. Scotti and D.C. Dunand, Freeze Casting—A Review of Processing, Microstructure and Properties Via the Open Data Repository, Freeze Casting.net, *Prog. Mater. Sci.*, 2018, **94**, p 243–305. https://doi.org/10.1016/j.pmatsci.2018.01.001
15. S. Deville, E. Saiz and A. Tomsia, Ice-Templated Porous Alumina Structures, *Acta Mater.*, 2007, **55**, p 1965–1974
16. S. Deville, A.P. Tomsia and S. Meille, Complex Composites Built through Freezing, *Acc. Chem. Res.*, 2022, **55**, p 1492–1502. https://doi.org/10.1021/acs.accounts.2c00064
17. T. Waschkies, R. Oberacker and M.J. Hoffmann, Investigation of Structure Formation During Freeze-Casting from Very Slow to Very Fast Solidification Velocities, *Acta Mater.*, 2011, **59**, p 5135–5145. https://doi.org/10.1016/j.actamat.2011.04.046
18. S. Deville, Freeze-Casting of Porous Ceramics: A Review of Current Achievements and Issues, *Adv. Eng. Mater.*, 2008, **10**, p 155–169. https://doi.org/10.1002/adem.200700270
19. I. Nelson and S.E. Naleway, Intrinsic and Extrinsic Control of Freeze Casting, *J. Mater. Res. Technol.*, 2019, **8**, p 2372–2385. https://doi.org/10.1016/j.jmrt.2018.11.011
20. A. Shaga, P. Shen, C. Sun and Q. Jiang, Lamellar-Interpenetrated Al-Si-Mg/SiC Composites Fabricated by Freeze Casting and Pressureless Infiltration, *Mater. Sci. Eng. A.*, 2015, **630**, p 78–84. https://doi.org/10.1016/j.msea.2015.02.012
21. R. Guo, H. Lv, P. Shen, Z. Hu and Q. Jiang, Lamellar-Interpenetrated Al−Si−Mg/Al2O3−ZrO2 Composites Prepared by Freeze Casting and Pressureless Infiltration, *Ceram. Int.*, 2017, **43**, p 3292–3297. https://doi.org/10.1016/j.ceramint.2016.11.162
22. R.F. Guo, N. Guo, P. Shen, L.K. Yang and Q.C. Jiang, Effects of Ceramic Lamellae Compactness and Interfacial Reaction on the Mechanical Properties of Nacre-Inspired Al/Al2O3–ZrO2 Composites, *Mater. Sci. Eng. A.*, 2018, **718**, p 326–334. https://doi.org/10.1016/j.msea.2018.01.088
23. C. Ferraro, S. Meille, J. Réthoré, N. Ni, J. Chevalier and E. Saiz, Strong and Tough Metal/Ceramic Micro-Laminates, *Acta Mater.*, 2018, **144**, p 202–215. https://doi.org/10.1016/j.actamat.2017.10.059
24. S. Roy, J. Frohnheiser and A. Wanner, Effect of Ceramic Preform Freeze-Casting Temperature and Melt Infiltration Technique on the Mechanical Properties of a Lamellar Metal/Ceramic Composite, *J. Compos. Mater.*, 2020, **54**, p 2001–2011. https://doi.org/10.1177/0021998319890661
25. S. Roy and A. Wanner, Metal/ceramic Composites from Freeze-Cast Ceramic Preforms: Domain Structure and Elastic Properties, *Compos. Sci. Technol.*, 2008, **68**, p 1136–1143. https://doi.org/10.1016/j.compscitech.2007.06.013
26. S. Roy, B. Butz and A. Wanner, Damage Evolution and Domain-Level Anisotropy in Metal/Ceramic Composites Exhibiting Lamellar

Microstructures, *Acta Mater.*, 2010, **58**, p 2300–2312. https://doi.org/10.1016/j.actamat.2009.12.015
27. S. Roy, J. Gibmeier and A. Wanner, In Situ Study of Internal Load Transfer In a Novel Metal/Ceramic Composite Exhibiting Lamellar Microstructure Using Energy Dispersive Synchrotron X-ray Diffraction, *Adv. Eng. Mater.*, 2009, **11**, p 471–477. https://doi.org/10.1002/adem.200800352
28. S. Roy, Metal/Ceramic Composites from Freeze-Cast Preforms: Domain Structure and Mechanical Properties, *Univ. Karlsr.*, 2009, **68**(5), p 1136–1143
29. P. Maurya, N. Kota, J. Gibmeier, A. Wanner and S. Roy, Review on Study of Internal Load Transfer in Metal Matrix Composites USING Diffraction Techniques, *Mater. Sci. Eng. A.*, 2022, **840**, 142973. https://doi.org/10.1016/j.msea.2022.142973
30. N. Chawla and K.K. Chawla, *Metal Matrix Composites*, Springer, New York, 2013
31. K.K. Chawla, *Composite Materials: Science and Engineering*, Springer, Fourth, 2019
32. S. Roy, P. Albrecht, L. Przybilla, K.A. Weidenmann, M. Heilmaier and A. Wanner, Effect of Phase Architecture on the Thermal Expansion Behavior of Interpenetrating Metal/Ceramic Composites, *Ceram. Trans.*, 2013, **240**, p 33–42
33. D. Hautcoeur, Y. Lorgouilloux, A. Leriche, M. Gonon, B. Nait-ali, D.S. Smith, V. Lardot and F. Cambier, Thermal Conductivity of Ceramic / Metal Composites from Preforms Produced by Freeze Casting, *Ceram. Int.*, 2016, **42**, p 14077–14085. https://doi.org/10.1016/j.ceramint.2016.06.016
34. Y. Tang, S. Qiu, M. Li and K. Zhao, Fabrication of Alumina/Copper Heat Dissipation Substrates by Freeze Tape Casting and Melt Infiltration for High-Power LED, *J. Alloy. Compd.*, 2017, **690**, p 469–477. https://doi.org/10.1016/j.jallcom.2016.08.149
35. M. Nakata and K. Suganuma, Effect of Internal Structure on Thermal Properties of Alumina/Aluminum Composites Fabricated by Gelate-Freezing and Partial-Sintering Process, Respectively, *Mater. Trans.*, 2005, **46**, p 130–135. https://doi.org/10.2320/matertrans.46.130
36. S. Roy, A. Nagel and K.A. Weidenmann, Anisotropic Thermal Expansion Behavior of an Interpenetrating Metal/Ceramic Composite, *Thermochim. Acta.*, 2020 https://doi.org/10.1016/j.tca.2019.178488
37. S. Roy, K.G. Schell, E.C. Bucharsky, K.A. Weidenmann, A. Wanner and M.J. Hoffmann, Processing and Characterization of Elastic and Thermal Expansion Behaviour of Interpenetrating Al12Si/Alumina Composites, *Mater. Sci. Eng. A.*, 2019 https://doi.org/10.1016/j.msea.2018.11.100
38. P. Jana, S. Ray, D. Goldar, N. Kota, S.K. Kar and S. Roy, Study of the Elastic Properties of Porous Copper Fabricated Via the Lost Carbonate Sintering Process, *Mater. Sci. Eng. A.*, 2022, **836**, 142713. https://doi.org/10.1016/j.msea.2022.142713
39. P. Jana, M.J. Oza, K.G. Schell, E.C. Bucharsky, T. Laha and S. Roy, Study of the Elastic Properties and Thermal Shock Behavior of Al–SiC-Graphite Hybrid Composites Fabricated by Spark Plasma Sintering, *Ceram. Int.*, 2022, **48**, p 5386–5396. https://doi.org/10.1016/j.ceramint.2021.11.082
40. D. Kaiser, B. de Graaff, S. Dietrich and V. Schulze, A Novel Procedure to Account for High Temperature Gradients in an Induction Dilatometer Sample During Rapid Heating, *Thermochim. Acta.*, 2016, **646**, p 8–15. https://doi.org/10.1016/j.tca.2016.10.014
41. A. Wanner, Elastic Modulus Measurements of Extremely Porous Ceramic Materials by Ultrasonic Phase Spectroscopy, *Mater. Sci. Eng. A.*, 1998, **248**, p 35–43. https://doi.org/10.1016/s0921-5093(98)00524-3
42. J. Berthelot, *Composite Materials: Mechanical Behavior and Structural Analysis*, Springer, New York, 1999
43. J.F. Nye, *Physical Properties of Crystals*, Oxford Science Publications, Oxford, 2006
44. F. Delannay, Thermal Stresses and Thermal Expansion in MMCs, in: Compr. Compos. Mater. V 2000
45. K. Lichtenberg and K.A. Weidenmann, Effect of reinforcement size and orientation on the thermal expansion behavior of metallic glass reinforced metal matrix composites produced by gas pressure infiltration, *Thermochim. Acta.*, 2017, **654**, p 85–92. https://doi.org/10.1016/j.tca.2017.05.010
46. T. Courtney, Mechanical Behavior of Materials, Waveland Press, Inc., 2005
47. W.D.J. Callister and D.G. Rethwisch, *Materials Science and Engineering - An Introduction*, John Wiley, New Jersey, 2009
48. G. Korb, J. Korab and G. Groboth, Thermal Expansion Behaviour of Unidirectional Carbon-Fibre-Reinforced Copper-Matrix Composites, *Compos. Part A Appl. Sci. Manuf.*, 1998, **29**, p 1563–1567
49. S.J. Kudela, A. Rudajevova and S. Kudela, Anisotropy of Thermal Expansion in Mg- and Mg4Li-Matrix Composites Reinforced by Short Alumina Fibers, *Mater. Sci. Eng. A.*, 2007, **462**, p 239–242. https://doi.org/10.1016/j.msea.2006.05.173
50. S. Ku, P. Luka and S. Ku, Anisotropy of the Thermal Expansion in Mg Fibre Composites, *Scr. Mater.*, 2005, **53**, p 1417–1420. https://doi.org/10.1016/j.scriptamat.2005.08.018
51. H.E. Nassini and M. Moreno, Thermal Expansion Behavior of Aluminum Alloys Reinforced with Alumina Planar Random Short Fibers, *J. Mater. Sci.*, 2001, **6**, p 2759–2772
52. S. Roy, A. Nagel and K.A. Weidenmann, Anisotropic thermal Expansion Behavior of an Interpenetrating Metal/Ceramic Composite, *Thermochim. Acta.*, 2020, **684**, 178488. https://doi.org/10.1016/j.tca.2019.178488
53. A. Mattern, Interpenetrierende Metall-Keramik-Verbundwerkstoffe mit isotropen und anisotropen Al2O3-Verstärkungen, University of Karlsruhe, 2004
54. T. Huber, H.P. Degischer, G. Lefranc and T. Schmitt, Thermal Expansion Studies on Aluminium-Matrix Composites with Different Reinforcement Architecture of SiC Particles, *Compos. Sci. Technol.*, 2006, **66**, p 2206–2217. https://doi.org/10.1016/j.compscitech.2005.12.012
55. T.A. Hahn and R.W. Armstrong, Internal Stress and Solid Solubility Effects on the Thermal Expansivity of Al-Si Eutectic Alloys, *Int. J. Thermophys.*, 1988, **9**, p 179–193. https://doi.org/10.1007/BF00504238
56. D.K. Balch, T.J. Fitzgerald, V.J. Michaud, A. Mortensen, Y. Shen and S. Suresh, Thermal Expansion of Metals Reinforced with Ceramic Particles and Microcellular Foams, Metall, *Mater. Trans. A Phys. Metall. Mater. Sci.*, 1996, **27P**, p 3700–3717
57. H. Boehm, H. Degischer, W. Lacom and J. Qu, Experimental and Theoretical Study of the Thermal Expansion Behavior of Aluminium Reinforced by Continuous Ceramic Fibers, *Compos. Eng.*, 1995, **5**, p 37–49
58. Y. Shen, Combined Effects of Microvoids and Phase Contiguity on the Thermal Expansion of Metal-Ceramic Composites, *Mater. Sci. Eng. A.*, 1997, **237**, p 102–108
59. A. Kelly, C. Zweben and T.W. Clyne, *Comprehensive Composite Materials Metal Matrix Composites*, Elsevier, UK, 2000
60. P. Turner, Thermal Expansion Stresses in Reinforced Plastics, 1946
61. E.H. Kerner, The Elastic and Thermo-Elastic Properties of Composite Media, *Proc. Phys. Soc. Sect. B.*, 1956, **69**, p 808–813
62. L.I. Tuchinskii, Thermal Expansion of Composites with A Skeletal Structure, *Powder Metall. Met. Ceram.*, 1983, **22**, p 659–664
63. R. Schapery, Thermal Expansion Coefficients of Composite Materials Based on Energy Principles, *J. Compos. Mater.*, 1968, **2**, p 380. https://doi.org/10.1177/002199836800200308
64. P.S. Turner, Thermal-expansion stresses in reinforced plastics, *J. Res. Natl. Bur. Stand.*, 1934, **37**(1946), p 239. https://doi.org/10.6028/jres.037.015
65. Granta Design Limited. CES EduPack 2011.2 Version 7.0. Computer-Software, (n.d.)
66. J. Roesler, H. Harders and M. Baeker, *Mechanisches Verhalten der Werkstoffe*, Teubner Verlag / GWV Fachverlage GmbH, Wiesbaden, Germany, 2006
67. S. Roy, K.G. Schell, E.C. Bucharsky, K.A. Weidenmann, A. Wanner and M.J. Hoffmann, Processing and Characterization of Elastic and Thermal Expansion Behaviour of Interpenetrating Al12Si/alumina Composites, *Mater. Sci. Eng. A.*, 2019, **743**, p 339–348. https://doi.org/10.1016/j.msea.2018.11.100

68. T. Huber, Thermal Expansion of Aluminum Alloys and Composites, TU Wien, 2003